catalysts

MDPI

Article

Band Gap Engineering in Quadruple-Layered Sillén–Aurivillius Perovskite Oxychlorides $Bi_7Fe_2Ti_2O_{17}X$ (X = Cl, Br, I) for Enhanced Photocatalytic Performance

Jikun Chen [1,†], Yan Gu [1,†], Shishi Xu [1], Yunxiang Zhang [1,*], Zhe Zhang [1], Lin Shi [1], Zhichao Mu [1], Chenliang Zhou [1], Jiali Zhang [1] and Qinfang Zhang [1,2,*]

[1] School of Materials Science and Engineering, Yancheng Institute of Technology, Yancheng 224001, China
[2] Jiangsu Provincial Key Laboratory of Eco-Environmental Materials, Yancheng Institute of Technology, Yancheng 224051, China
* Correspondence: chzyx123@163.com (Y.Z.); qfangzhang@gmail.com (Q.Z.)
† These authors contributed equally to this work.

Abstract: Developing efficient photocatalyst for the photoreduction of CO_2 and degradation of organic pollutants is an effective alternative to address increasingly serious energy problems and environmental pollution. Herein, the isostructural Sillén–Aurivillius oxyhalides, $Bi_7Fe_2Ti_2O_{17}X$ (X = Cl, Br, and I; BFTOX), are fabricated for CO_2 reduction and degradation of organic pollutants for the first time. Density functional theory (DFT) calculations show that the valence band maximum (VBM) of BFTOC and BFTOB is contributed by the dispersive 2*p* orbitals of O-atoms, providing the narrow band gap (E_g) and possibly the stability against self-decomposition deactivation. The photocatalytic activities of BFTOX are strongly affected by the halogens (Cl, Br, and I), namely, the BFTOCl sample displays outstanding activity improvement (3.74 $\mu mol \cdot g^{-1} \cdot h^{-1}$) for photocatalytic performance. This is mainly attributed to the high separation of charge carriers, small optical band gap, and extended optical absorption. This work focuses on affording a reference to develop efficient and stable photocatalysts from Sillén-Aurivillius layered oxyhalide materials.

Keywords: Sillén–Aurivillius; $Bi_7Fe_2Ti_2O_{17}X$; photocatalyst; degradation; CO_2 reduction

Citation: Chen, J.; Gu, Y.; Xu, S.; Zhang, Y.; Zhang, Z.; Shi, L.; Mu, Z.; Zhou, C.; Zhang, J.; Zhang, Q. Band Gap Engineering in Quadruple-Layered Sillén–Aurivillius Perovskite Oxychlorides $Bi_7Fe_2Ti_2O_{17}X$ (X = Cl, Br, I) for Enhanced Photocatalytic Performance. *Catalysts* **2023**, *13*, 751. https://doi.org/10.3390/catal13040751

Academic Editor: Marcos Fernández García

Received: 21 February 2023
Revised: 4 April 2023
Accepted: 12 April 2023
Published: 14 April 2023

1. Introduction

With the development of industrialization, environmental problems have become a global issue of general concern in modern society, particularly for the greenhouse effect caused by carbon dioxide (CO_2) and the discharge of various organic pollutants, threatening the survival and development of mankind [1,2]. Photocatalytic technology is an appealing solution for the reduction of CO_2 and the removal of organic pollutants due to its ability to reduce them into high value-added chemicals or completely harmless molecules under sunlight or UV irradiation [3–6]. Moreover, semiconductor photocatalysis has attracted wide attention from researchers with the advantages of low cost, highly efficient, recyclable and does not lead to secondary pollution [7,8]. However, most photocatalytic materials have the problems of wide band gap, serious photogenerated carrier recombination and poor stability under light irradiation [9–12]. Thus, it is necessary to develop new efficient and stable visible light (VL) photocatalysts.

In recent years, bismuth (Bi)-based materials show the potential to be a novel series for VL responsive photocatalysts [13–16]. Consequently, large amounts of Bi-based photocatalysts have been studied, such as Bismuth trioxide (Bi_2O_3) [17,18], BiOX (X = Cl, Br, and I) [19–21], $Bi_4Ti_3O_{12}$ [22,23], and Bi_4MO_8X (M = Nb, Ta; X = Cl, Br) [24,25], etc. Among them, Sillén–Aurivillius layered oxyhalide materials, such as Bi_4MO_8X (M = Nb, Ta; X = Cl, Br), which are composed of $[MO_6]$ and $[(Bi_2O_2)_2X]$ blocks, have attracted considerable interest for photocatalysis with the virtues of the narrower band gap (E_g), ferroelectric polarization, layered crystal structure and stability against self-decomposition deactivation [26–28]. In 2016, Hironori Fujito et al. fabricated Bi_4NbO_8Cl successfully from Bi_2O_3, BiOCl, and Nb_2O_5 powders and the photocatalytic performance for oxygen (O_2) evolution was also evaluated in methanol solution [25]. Simultaneously, their density functional theory (DFT) calculations demonstrated that the valence band maximum (VBM) of Sillén–Aurivillius layered oxyhalide materials is mainly from O-2*p* orbitals [29,30]. This material can avoid the self-decomposition phenomenon of catalysts upon light irradiation because of the high oxidation of stable by the photo-excited holes near VBM [28,31]. Then, Xiaoping Tao et al. proved that Bi_4TaO_8Cl can be used for hydrogen (H_2) evolution under VL irradiation [32]. These results indicate that Sillén–Aurivillius layered oxyhalide materials Bi_4MO_8X (M = Nb, Ta; X = Cl, Br) should be a potential novel visible light photocatalyst material. In recent years, Sillén–Aurivillius materials were further extensively studied, such as the construction of heterojunctions [33,34], surface plasmon nanoparticle modification [26,35], element doping [27,36], etc., which proves that this materials have great development potential for photocatalysis, for example $Bi_7Fe_2Ti_2O_{17}X$ (X = Cl, Br, I) (BFTOX). In 2022, Yan Gu et al. fabricated $Bi_7Fe_2Ti_2O_{17}Cl$ successfully by using a one-step flux route and solid-state reaction, and its degradation efficiency of tetracycline (TC) reaches 90% within 90 min, which confirms that BFTOX should be a potential novel visible light photocatalyst material [37].

In order to further advance the development of Bi-based oxyhalides semiconductor materials, a series of novel Sillén–Aurivillius layered oxyhalide materials, $Bi_7Fe_2Ti_2O_{17}X$ (X = Cl, Br, I) (BFTOX), have been successfully synthesized via a molten-salt method by using the BiOX (X = Cl, Br, and I) precursor powders. Originally, we display the investigation of material characteristics, such as the band structure, effective mass, lattice constant, and E_g of BFTOX influenced by the halogen, Cl, Br, and I, from density functional theory (DFT) calculation. Then, material properties of BFTOX powders are determined by characterization techniques of X-ray diffraction (XRD), scanning electron microscope (SEM), energy dispersive spectroscopy (EDS), and X-ray photoelectron spectroscopy (XPS). Furthermore, the photocatalytic activities of different samples are compared by the reduction of CO_2 and the degradation of methyl orange (MO) and Rhodamine B (RhB), and BFTOX exhibits the best photocatalytic performance. In addition, the possible photocatalysis mechanisms of BFTOX have also been discussed in detail.

2. Results and Discussion

2.1. DFT Calculations

The structure of Sillén-Aurivillius materials is composed of fluorite ($[Bi_2O_2]^{2+}$) [20], like-perovskite ($[A_{n-1}B_nO_{3n+1}]^{3-}$) [21], and halogen ([X]) with the general formula of $[Bi_2O_2]^{2+}[X]^{-}[Bi_2O_2]^{2+}[A_{n-1}B_nO_{3n+1}]^{3-}$ [22], where n represents the number of perovskite layers ($n = 1, 2, 3 \ldots$). Meanwhile, with the number of perovskite layers increasing, the difficulty of implementation will also increase, whether in calculation or experiment. After drawing on many previous works, this work put a sight on comparing three quadruple-perovskite layers semiconductor photocatalysts, $Bi_7Fe_2Ti_2O_{17}X$ (X = Cl, Br, I). The layers are constructed in the Cmcm space group (No. 63), aiming to provide the high efficiencies of photocatalysts for the reduction of CO_2 and degradation of organic pollutants. The crystal structure of BFTOX in Figure 1a shows that the novel BFTOX is an $n = 4$ member of Sillén–Aurivillius type perovskite oxyhalides with alternate stacking of Aurivillius perovskite blocks ($[Bi_3Ti_2Fe_2O_{13}]^{3-}$) and Sillén blocks ($[(Bi_2O_2)_2X]^{3+}$).

In order to further investigate the electronic properties of BFTOX, the energy band structure plots are displayed in Figure 1b–d. We can find that all BFTOX samples belong to the indirect-gap semiconductor. The calculated E_g values of BFTOC, BFTOB, and BFTOI are 2.30 eV, 2.44 eV, and 2.65 eV, respectively. As the halogen atomic number increases from Cl to Br and I, the band gap gradually widens, which may be related to the electronegativity of the halogen atoms. Furthermore, the electronegativity of materials also influences the energy level of the halogen atoms that elements with low electronegativity have high energy level positions, and thus the halogen level (Cl 3*p*, Br 4*p* and I 5*p*) increases as the atomic number increases relative to the O 2*p* orbitals. Quite unexpectedly, the VBM of BFTOC and BFTOB is predominantly composed of O 2*p* orbitals, while that of BFTOI is contributed by I 5p orbitals. For BFTOI, the VBM contribution is similar to that of simple oxyhalides BiOCl and BiOBr. During photocatalytic process, it is inevitable to be oxidized by the holes excited by the light, and the stability will be poor [20]. When it comes to BFTOC and BFTOB, the VBM is mainly composed of the dispersive O 2*p* orbitals. Meanwhile, the calculated effective masses of all samples in Table 1 confirm that the lower values of BFTOC and BFTOB. Hence, we believe that the excited holes in the stable oxygen anion near the VBM of both materials can effectively oxidize water without inactivation due to self-decomposition phenomenon of catalysts upon light irradiation.

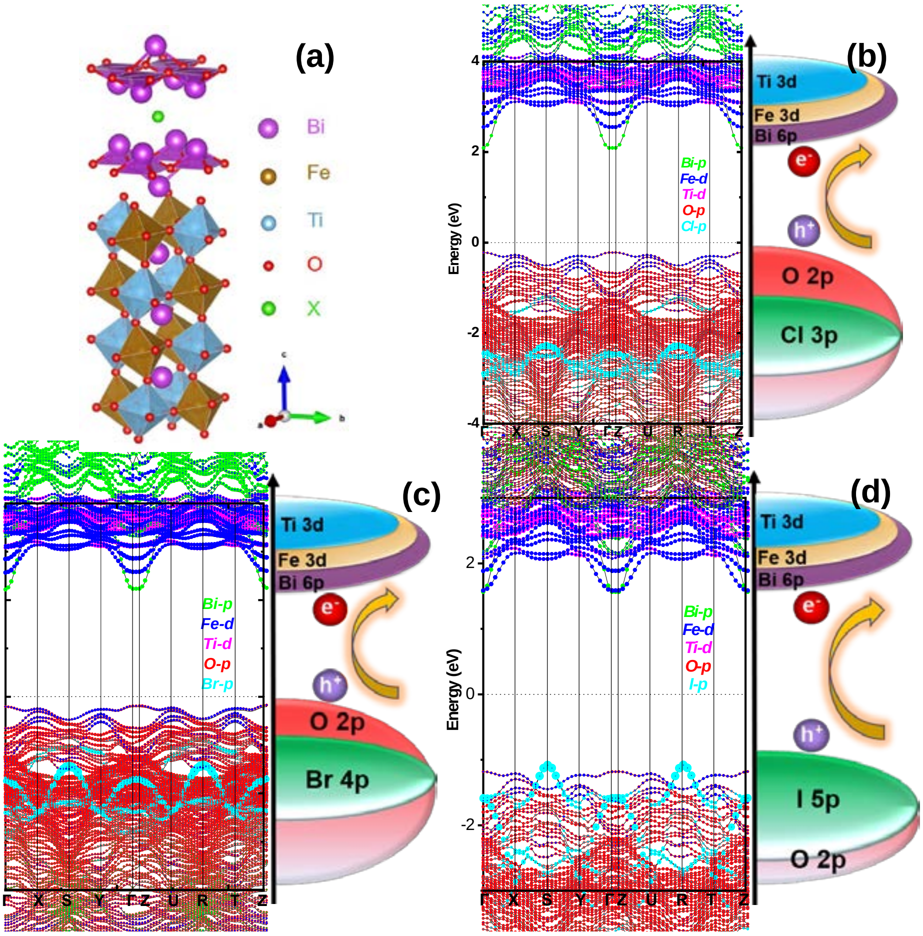

Figure 1. (**a**) Crystal structure of BFTOX. Band structures of (**b**) BFTOC, (**c**) BFTOB and (**d**) BFTOI.

Table 1. Calculated effective masses (unit m_0) of the electrons and holes of BFTOC, BFTOB and BFTOI by different directions.

	BFTOC		BFTOB		BFTOI	
Effective Mass	**Electron**	**Hole**	**Electron**	**Hole**	**Electron**	**Hole**
m_{xx} ($\Gamma - X$)	0.023	0.181	0.013	0.131	0.053	
m_{yy} ($\Gamma - Y$)	0.035	0.099	0.018	0.098	0.054	
m_{zz} ($\Gamma - Z$)	9.879	7.904	19.004	6.228	5.137	
m_{xx} ($S - Y$)						0.035
m_{yy} ($S - X$)						0.031

2.2. Material Properties of BFTOX (X = Cl, Br, and I)

The crystalline phases of as-prepared BFTOX powders were determined by XRD technology, and the corresponding results are displayed in Figure 2a–c. It can be observed that the diffraction peaks at 30.58°, 32.65°, 46.73°, and 56.97° can be indexed to the (116), (020), (220), and (316) crystal planes of BFTOX samples, which are all consistent with the calculated cards from DFT. These results confirm that BFTOX (X = Cl, Br, and I) materials are well-crystallized after calcination at different high temperatures in this experiment. Moreover, from the DFT results in Figure 1a, the structure of BFTOX (X = Cl, Br, and I) is the orthorhombic structure along with the space group of P21cn. In this case, the experimental lattice constants of BFTOX are calculated (BFTOC: a = 5.508 Å, b = 5.481 Å, and c = 26.593 Å; BFTOB: a = 5.501 Å, b = 5.478 Å, and c = 26.592 Å; BFTOI: a = 5.492 Å, b = 5.478 Å, and c = 26.644 Å). These results and the theoretically calculated lattice constants in Figure 2a–c are extremely similar, further indicating the successful preparation of BFTOX.

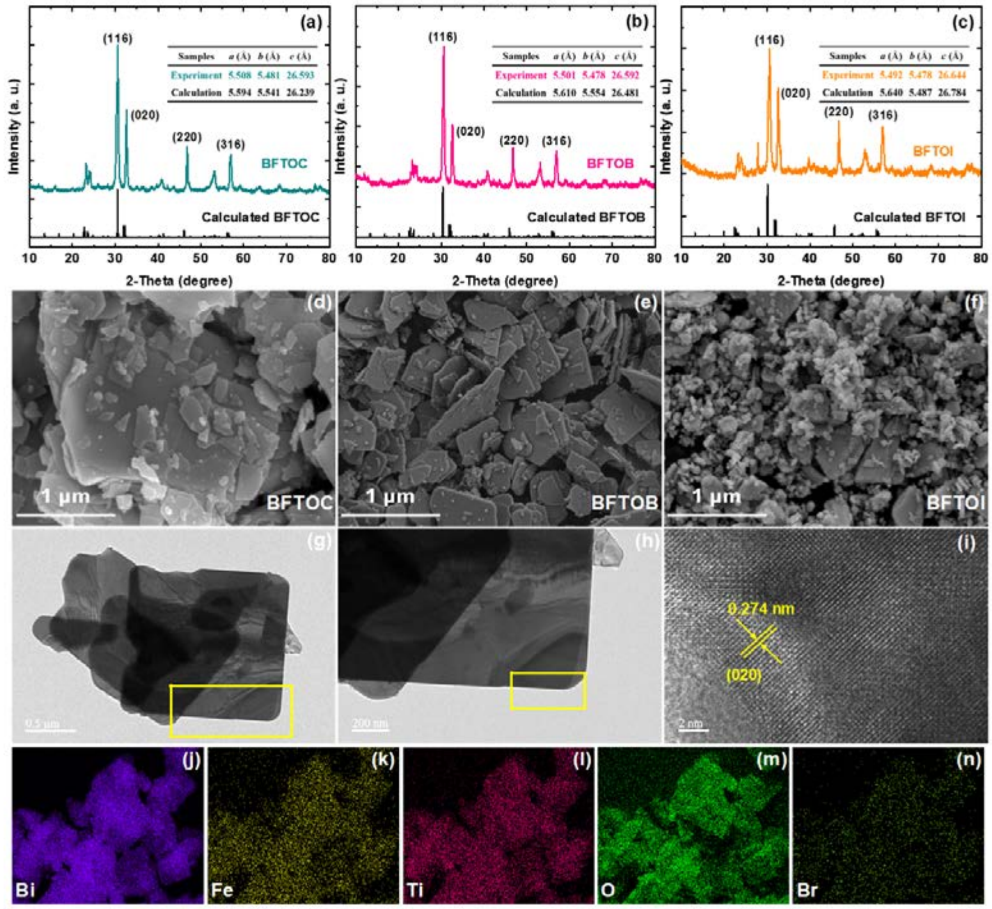

Samples	a (Å)	b (Å)	c (Å)
Experiment	5.508	5.481	26.593
Calculation	5.594	5.541	26.239

Samples	a (Å)	b (Å)	c (Å)
Experiment	5.501	5.478	26.592
Calculation	5.610	5.554	26.481

Samples	a (Å)	b (Å)	c (Å)
Experiment	5.492	5.478	26.644
Calculation	5.640	5.487	26.784

Figure 2. XRD patterns and their corresponding calculated cards of (**a**) BFTOC, (**b**) BFTOB, and (**c**) BFTOI. SEM images of (**d**) BFTOC, (**e**) BFTOB, and (**f**) BFTO-I. (**g**) TEM and the corresponding HRTEM of (**h**,**i**) BFTOC nanoplates in yellow squares. The corresponding SEM-EDS elemental mappings of (**j**) Bi, (**k**) Fe, (**l**) Ti, (**m**) O, and (**n**) Br for BFTOB sample.

Afterwards, the microstructure of the as-prepared BFTOX samples is determined by using SEM. As depicted in Figure 2d–f, all samples possess a nanoplate-like structure, which may be caused by the weak Van der Waals' force between the halogen layer [X] and the fluorite layer [Bi_2O_2]. Meanwhile, the size of nanoplates of BFTOX samples gradually decreased from the halogen variation in Sillén–Aurivillius material, particularly for BFTOI. One possible reason for this phenomenon is the stability of the material structure. Because the iodine element (I) is easy to sublimate during the high temperature calcination process, it is easy to destroy the crystal structure, so the crystallinity is poor and it is easy to form nano-agglomerates. In addition, the SEM-EDS mappings of BFTOB nanoplates in Figure 2g–k confirm the existence of Bi, Fe, Ti, O, and X and they are evenly distributed on the whole nanoplates. A similar phenomenon is also observed in BFTOC and BFTOI samples, seen the supporting information in Figure S1. These further demonstrate the successful synthesis of the BFTOX materials.

The elements of Bi, Fe, Ti, O and Br are found in the survey XPS spectra of BFTOBr (Figure 3a), which is in accordance with the results of SEM-EDS. The peaks at about 159.10 and 164.42 eV in Figure 3b, obtained from BFTOB, are ascribed to the Bi $4f_{7/2}$ and Bi $4f_{5/2}$ of Bi^{3+} [38]. In the Fe $2p$ region of BFTOB (Figure 3c), there were two peaks at 711.09 and 725.36 eV, referring to Fe $2p_{1/2}$ and Fe $2p_{3/2}$, respectively, manifesting the existence of Fe^{3+} ions [39]. There were two fitted Ti 2p peaks centered at 458.12 and 465.73 eV in Figure S2, which were attributed to Ti $2p_{3/2}$ and Ti $2p_{1/2}$ to the oxidation state of Ti^{4+} [40,41]. The O 1s peaks at binding energies of 529.50, 530.17 and 531.99 eV, which arises from the Bi-O, Fe-O and Ti-O, respectively (Figure S3). In addition, the binding energy peaks of Br $3d_{5/2}$ and Br $3d_{3/2}$ are located at 68.46 and 79.45 eV, respectively (Figure 2d) [42,43].

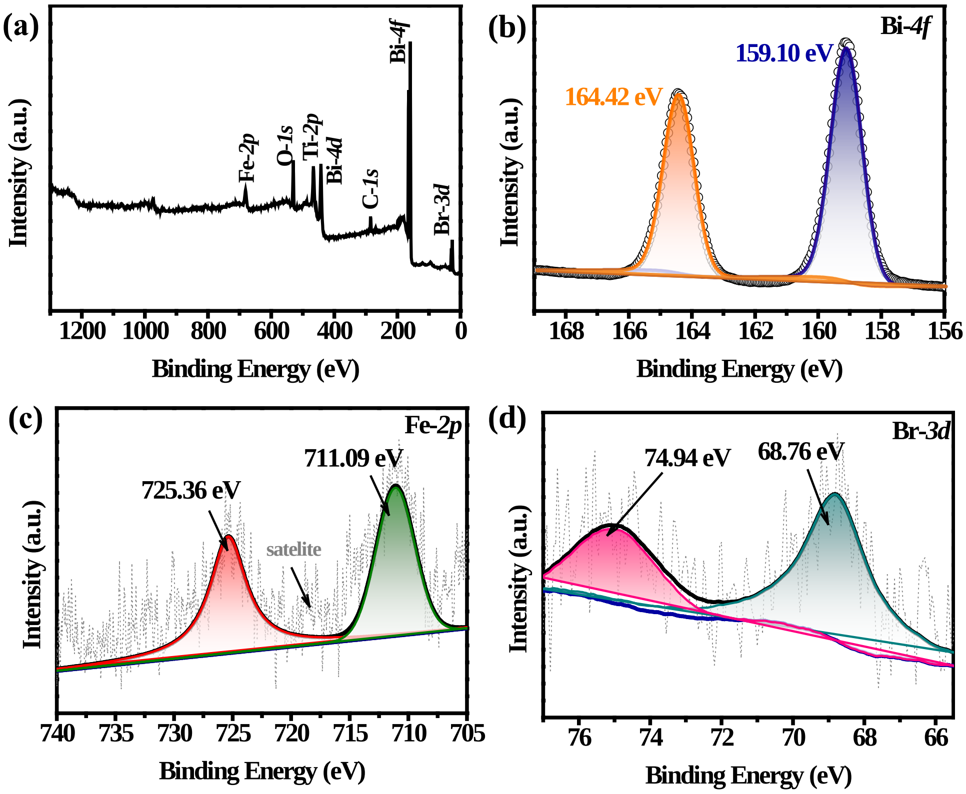

Figure 3. (**a**) XPS survey spectra of BFTOB corresponding to Bi, Fe, Ti, O and Br. High resolution XPS spectra of (**b**) Bi $4f$, (**c**) Fe $2p$, and (**d**) Br $3d$ of BFTOB, respectively.

2.3. Photocatalytic CO_2 Reduction Performance for BFTOX Materials

In order to evaluate the photocatalytic activities of BFTOX affected by the halogens, Cl, Br, and I, we conducted CO_2 reduction under the light irradiation. Under the simulated sunlight illumination, all BFTOX (X = Cl, Br, and I) samples can reduce the CO_2 to carbon monoxide (CO) in a sealed gas-solid phase reaction vessel without any organic sacrificial reagent. Figure 4a–c displays the relatively steady CO yields as a function of the irradiation time generated by BFTOC, BFTOB, and BFTOI. The yield values are about 14 μmol, 12 μmol, and 10 μmol for 210 min, respectively. To compare the performance clearly, the average yields of CO in 3.5 h are calculated in Figure 4d. It can be observed that the production rate of CO for BFTOC and BFTOB are 3.74 $\mu mol\ g^{-1}\ h^{-1}$ and 3.6 $\mu mol\ g^{-1}\ h^{-1}$, which are approximately 1.4 times higher than that of BFTOI (2.66 $\mu mol\ g^{-1}\ h^{-1}$). This result means that the trend of photocatalytic activities of BFTOX is BFTOC > BFTOB > BFTOI. The decrease in the CO production rate for samples may be related to the absorption of solar photons.

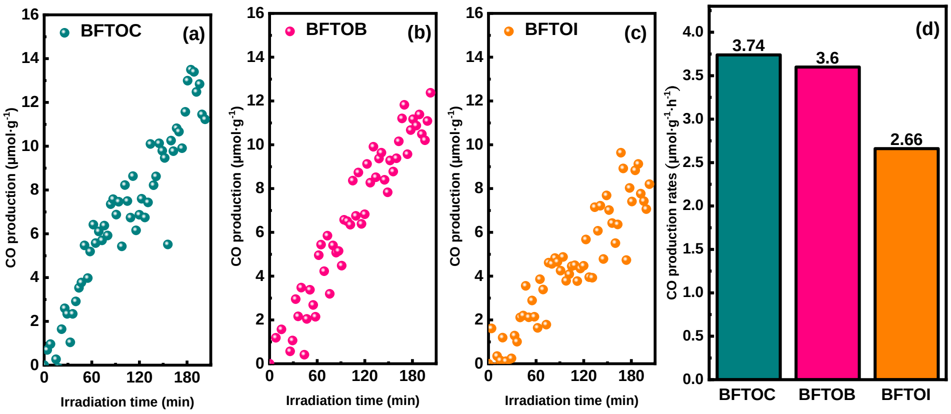

Figure 4. CO production of (**a**) BFTOC, (**b**) BFTOB, and (**c**) BFTOI, respectively. (**d**) The average CO production rates of BFTOX (X = Cl, Br, and I).

Subsequently, the UV–Vis diffuse absorbance spectrum (*DRS*) is used to evaluate the light absorption of BFTOX samples. It can be seen that all samples exhibit a strong photoresponse in the range of 390–550 nm in Figure 5a, which indicates that the BFTOX (X= Cl, Br, and I) materials are visible light catalysts. It is observed also that, the order of light response intensities is BFTOC > BFTOB > BFTOI, which can be ascribed to the sub-band gap absorption of powder materials. As we know, the significant sub-band gap absorption of films is indicative of the presence of the secondary phases or the band tailing [44–47]. This observation suggests the BFTOC powder has the lowest defect concentrations and photogenerated carrier recombination compared with the two other samples, which should be the reason for the highest performance of CO_2 reduction for BFTOC sample, as is consistent with the SEM results.

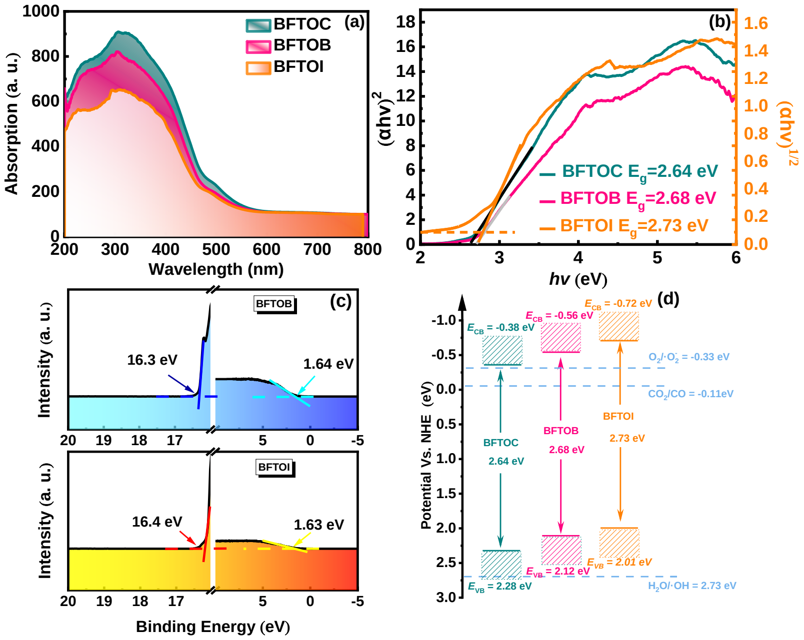

Figure 5. (**a**) UV-vis diffuse reflectance spectrum (*DRS*) of BFTOX (X = Cl, Br, and I) samples. (**b**) The calculated E_g of BFTO-X from Tauc's band-gap plots. (**c**) UPS valence band spectra of BFTOBr and BFTOI; (**d**) The energy band structure of BFTOX (X = Cl, Br, and I).

In addition, the BFTOC powder has the lowest defect concentrations compared with the two other samples. This should be the reason for the highest performance of CO_2 reduction for BFTOC sample, as is consistent with the SEM results. Furthermore, as the atomic number of the halogen increases in BFTOX (X = Cl, Br, and I), the absorption edge decreases, thus widening the E_g of samples. For a clearer comparison, the E_g values are determined by applying the Kabelka-Munk function [48–50]:

$$(\alpha h v)^{1/m} = A\left(hv - E_g\right) \tag{1}$$

where A, α, and hv are constant, absorption coefficient, and photon energy, respectively. The constant m is connected with the type of materials: the direct-gap semiconductor or the indirect-gap semiconductor [49]. From DFT calculation results, BFTOX is an indirect-gap semiconductor. Therefore, the value of m is 2. By the linear intersection in Figure 5b, the corresponding E_g values of BFTOX (X = Cl, Br, and I) are 2.64 eV, 2.68 eV, and 2.74 eV, respectively. This result is consistent with the trend of DFT calculation, as depicted in Figure 1.

In general, the positions of the valence band maximum (VBM) and conduction band minimum (CBM) of photocatalysts determines the photocatalytic activities of CO_2 reduction under light irradiation. Here, ultraviolet photoelectron spectroscopy (UPS) is employed to clarify the VBM and CBM positions of BFTOX samples, and the results of BFTOB and BFTOI are shown in Figure 5c. The result of BFTOC can be found in our previous work [44]. It can be calculated that the values of secondary cutoff energy ($E_{\text{cut-off}}$) of BFTOX are 16.30 eV, 16.30 eV, and 16.40 eV, respectively. And the position energy of corresponding Fermi levels (E_F) can be deduced from the equation [49]:

$$\varphi = hv - E_{\text{cut}-\text{off}} \tag{2}$$

where hv is about 21.22 eV for the He I electron energy. Therefore, the E_F values of BFTOC, BFTOB, and BFTOI are 4.92 eV, 4.92 eV, and 4.82 eV, respectively. In addition, the on-set energy ($E_{\text{on-set}}$) of samples can be applied to determining the gap between valence band and E_F. From Figure 5c, the $E_{\text{on-set}}$ values of BFTOC, BFTOB, and BFTOI are 1.80 eV, 1.64 eV, and 1.63 eV. Therefore, the valence band positions of these samples are 6.72 eV, 6.56 eV, and 6.45 eV, respectively. As the E_g values are depicted in Figure 5b, the conduction band positions are 4.06 eV, 3.88 eV, and 3.72 eV from the equation that $E_{CB} = E_{VB} - E_g$. According to previous works, the relationship between the vacuum energy (E_{abs}) and the normal electrode potential (E^{Θ}) can be described as follows [51]:

$$E_{abs} = -E^{\Theta} - 4.44 \tag{3}$$

Correspondingly, the valence band positions of BFTOC, BFTOB, and BFTOI (vs. NHE) are 2.28 eV, 2.12 eV, and 2.01 eV, while the valence band positions of samples are -0.38 eV, -0.56 eV, and -0.72 eV, respectively. Based on the above discussions, the energy band diagrams of the CBM and VBM potentials for BFTOX samples are exhibited in Figure 5d. We can find that as the halogen in BFTOX is substituted from Cl to I, both the conduction and valence bands of samples are shifted upward. Meanwhiles, the E_g values are increased from 2.64 eV to 2.74, this result means that the widening of the band gap is mainly due to the shifting of the conduction band. Since the CBM of BFTOX (-0.38 eV, -0.56 eV, and -0.72 eV) are more negative than that of the CO_2/CO (-0.11 eV) redox potential, it confirms that the valence bands of BFTOX (X = Cl, Br, and I) are capable of CO_2 reduction, as the results in Figure 4.

In general, the size of photocatalyst nanoplates can directly affect the photocatalytic activity. When the nanoplate size is smaller, the number of nanoplates per unit mass is larger, and the specific surface area is larger. According to SEM results in Figure 2, the size of nanoplates of BFTOX samples gradually decreased from the halogen variation in Sillén–Aurivillius material, particularly for BFTOI. These results indicate that the BFTOI sample has the largest specific surface area, and it should have the maximum photocatalytic efficiency. However, this result is the opposite, which may be related to the generation and recombination of photogenerated charge carriers. As we know, the photocatalytic performance of BFTOX samples is affected by many factors, such as the separation and transfer of photogenerated electrons and holes. Here, photoelectrochemical characterizations, transient photocurrent densities (TPC) and electrochemical impedance spectra (EIS), are employed to investigate the charge transfer capability of the catalysts. Figure 6a shows the photocurrent response curves of BFTOX under light irradiation. It can be found that the trend of the photocurrent density of BFTOC is BFTOC > BFTOB > BFTOI. This result reveals the higher efficient separation of photo-generated electrons and holes for the BFTOC sample. Meanwhiles, a similar conclusion is also observed in the results of EIS in Figure 6b. The diameter of the arc radius of BFTOC on the EIS is much smaller that these of BFTOB and BFTOI, indicating that BFTOC sample possesses a faster transfer of the photo-generated electrons and holes. This excellent performance of separation and transfer of photogenerated carriers for BFTOC can be related to the highest quality of powder material along with the lowest defect concentrations, as exhibited in Figure 5a. In addition, the calculated effective masses of the electrons and holes in Table 1 shows that the values of BFTOB is smallest than other two samples, it suggests that the electron-hole pair recombination of BFTOB should be lowest and the BFTOB sample possesses the highest photocatalytic efficiency. However, the sample with the highest photocatalytic efficiency is BFTOC in experiment. The reason for this result is that the BFTOC sample has higher crystallization compared with the other two samples.

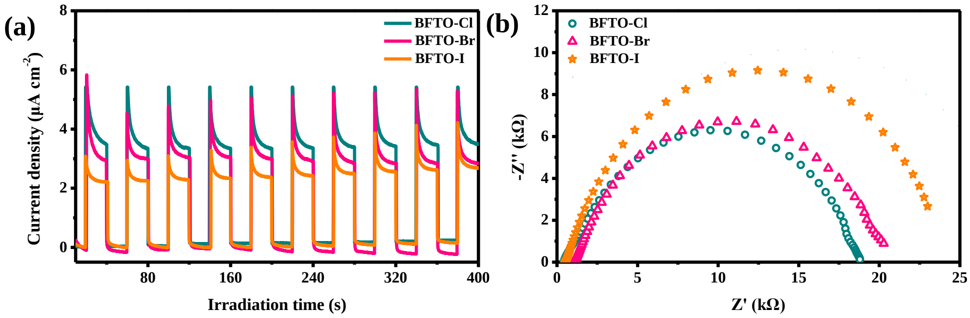

Figure 6. (**a**) Transient photocurrent densities and (**b**) EIS Nyquist plots of BFTOX (X = Cl, Br, and I).

2.4. *Photocatalytic Activity Enhancement Mechanism for the Photodegradation of Organic Pollutants*

The photocatalytic activities of BFTOX samples are also measured by using MO and RhB (10 mg/L) as the simulated pollutant under light irradiation, the results are displayed in Figure 7. To get a clear contrast, the degradation efficiencies of MO and RhB by BFTOX at different concentrations are calculated by the following equation [36]:

$$\eta = (C_0 - C) \ / \ C_0 \times 100\% \tag{4}$$

where C and C_0 are the sampling concentration of the reaction solution at different times and the initial concentration of MO and RhB solutions before light irradiation, respectively. From Figure 7a, we can find that the trend of degradation efficiencies for MO is BFTOC > BFTOB > BFTOI, and its result is similar for that of RhB solutions. Moreover, according to the fitting of pseudo-first-order: $\ln(C_0/C) = kt$, the degradation constants (k) are evaluated, as depicted in Figure 7b.

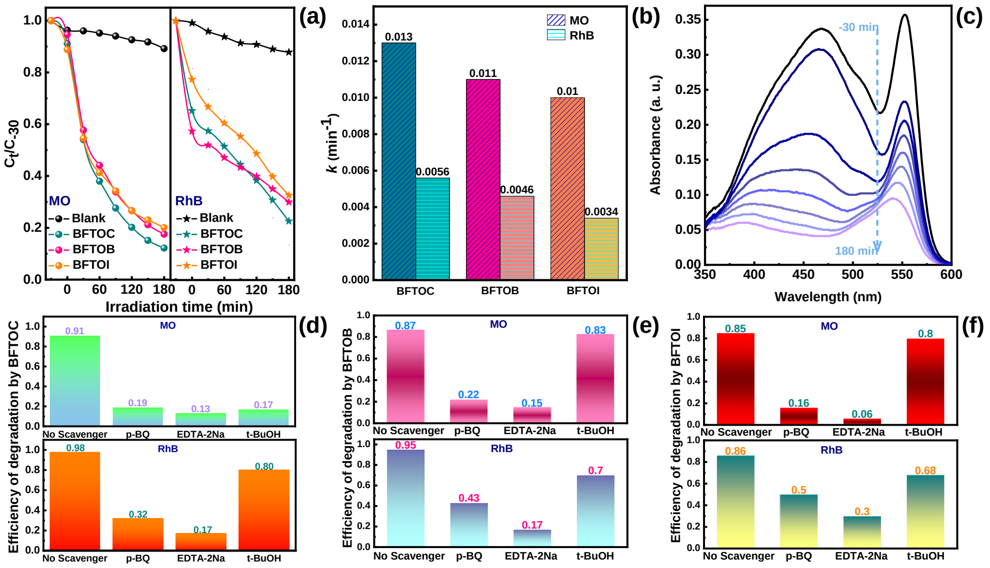

Figure 7. (**a**) The photocatalytic MO and RhB degradation activities over BFTOX. (**b**) The corresponding *k* values from kinetic linear fitting curves. (**c**) Degradation of the mixture of MO and RhB as a function of irradiation time. Degradation rate of MO/RhB over (**d**) BFTOC, (**e**) BFTOB, and (**f**) BFTOI with the addition of p-BQ, EDTA-2Na and TBA.

For MO, the BFTOC sample exhibits the highest apparent rate constant of about 0.011 min^{-1}, which is around 1.18 and 1.30 times of bare BFTOB and BFTOI samples, respectively. In addition, it can be observed that the degradation efficiencies of MO over BFTOX are higher than that of RhB, which indicates that that photocatalytic degradation of BFTOC powder is best, particularly for MO. Besides, BFTOC sample was also used to degrade the MO and RhB mixed pollutants, and its result is shown in Figure 7c. Obviously, the degradation efficiencies of MO at the wavelength of approximately 460 nm is higher compared with that of RhB at 550 nm. This further confirms the above conclusions. More importantly, the degradation efficiency of the mixture of MO and RhB is higher than that of single MO, which might be ascribed to the electrostatic force promoted the degradation of MO [52]. Moreover, the degradation efficiency of the mixture of MO and RhB is lower than that of single RhB due to the active sites of BFTOX being encircled intermediates, decelerating the production of electro-hole pairs and restraining the formation of radicals. In addition, the degradation efficiencies of MO are also higher than that of RhB in the mixture of MO and RhB. Namely, the degradation rates of MO over the BFTOX nanoplates are always higher than those of RhB, it may be mainly attributed to the molecular structure of oxychlorides, which needs further research in the future.

Afterwards, the active species trapping experiments of BFTOX (X = Cl, Br, and I) were carried out under light irradiation to evaluated the exact photocatalytic degradation mechanism. Radical scavenging materials, such as BQ, EDTA-2Na and TBA, are employed as the scavengers of ·OH, h$^+$, and $\cdot O_2^-$, respectively. The results in Figure 7d exhibit that the degradation efficiencies of MO and RhB over BFTOC are significantly inhibited under BQ and EDTA-2Na, while TBA only slightly reduces the degradation. In addition, similar capture trends are also found for BFTOB (Figure 7e) and BFTOI (Figure 7f). Therefore, h$^+$ and $\cdot O_2^-$ should be the major active species for MO and RhB degradation by BFTOC.

In fact, the stability and durability of photocatalysts is very important in practical applications. Figure 8a exhibits that the RhB degradation efficiency over BFTOC nanoplates with the same photocatalyst for five cycles. It can be found that the excellent photocatalysis performance of BFTOC is still significant after five cycles use, which confirms that the good recycling ability of BFTOC nanoplates. In addition, the stability of sample was also ascertained from XRD pattern in Figure 8b. The crystallinity of the as-prepared sample is similar to that of the used samples, it indicates that BFTOC nanoplates have the potential for the practical applications.

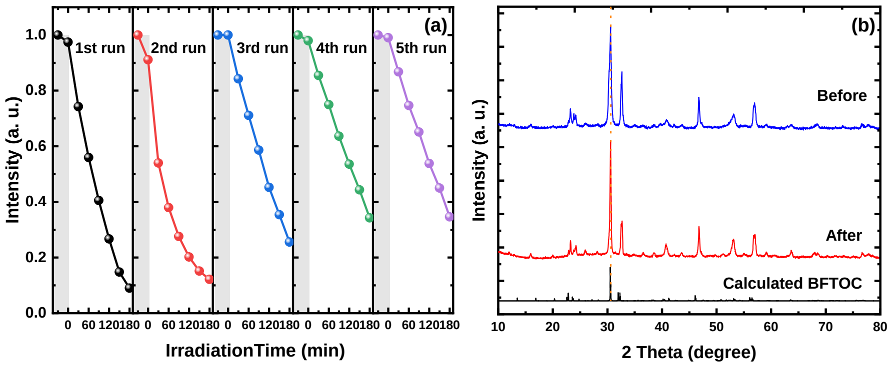

Figure 8. Time profiles of RhB degradation for five successive cycles with BFTOC in the photocatalytic process (**a**) and its XRD patterns (**b**).

Based on the aforementioned discussions, the probable photocatalytic degradation mechanism of organic pollutants over BFTOX materials is proposed in Figure 9. Under the light illumination, the e^- and h^+ will be produced on the CBM and VBM of BFTOX. The accumulated e^- on the CBM of BFTOX readily can reduce oxygen to $\cdot O_2^-$, which has more negative potentials (-0.38 eV, -0.56 eV, and -0.72 eV vs. NHE) than the O_2/O_2^- redox potential (-0.33 eV vs. NHE). The reason why ·OH ions do not contribute to the photocatalytic degradation process of organic pollutants is that in the acidic reaction solution, the E_{VB}s of BFTOX (BFTOC 2.28 eV; BFTOB 2.12 eV; BFTOI 2.01 eV) are more negative than the redox potential of $H_2O/\cdot OH$ (2.73 eV), and photogenerated holes cannot induce H_2O to ·OH, as shown in Figure 5d. Finally, the free radicals $\cdot O_2^-$ and e^-, which migrate to the surface of the powder and have good oxidation ability, directly degrade MO and RhB molecules into oxidation products. The possible photocatalytic mechanism of BFTOX powders can be described as follows:

$$Bi_7Fe_2Ti_2O_{17}X\ (X = Cl,\ Br,\ and\ I) + hv + (ultrasound)\ \rightarrow\ e^- + h^+ \tag{5}$$

$$O_2 + e^-\ \rightarrow\ \cdot O_2^- \tag{6}$$

$$\cdot O_2^- + h^+ + RhB/MO \rightarrow\ Intermediates + CO_2\ +\ H_2O \tag{7}$$

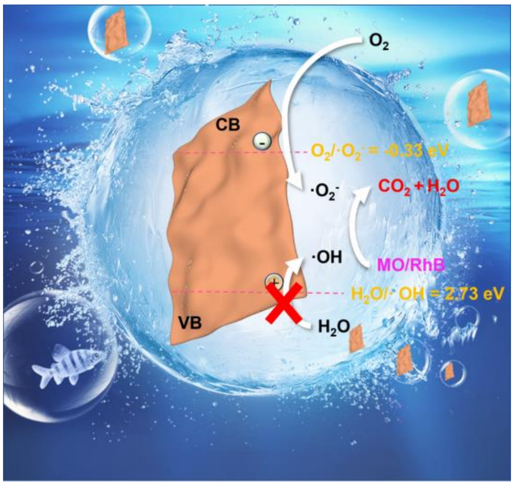

Figure 9. Schematic illustration of the proposed photocatalytic mechanism in the BFTOX powders.

3. Materials and Methods

3.1. Materials

Bismuth trioxide (Bi_2O_3) was purchased from Shanghai Aladdin Biochemical Technology CO., Ltd. Ferric oxide (Fe_2O_3) was purchased from Shanghai Shanpu Chemical Co., Ltd., Shanghai, China. Titanium dioxide (TiO_2), polyethylene glycol (EG), potassium chloride (KCl), potassium bromide (KBr), potassium iodide (KI), sodium chloride (NaCl), sodium bromide (NaBr), and sodium iodide (KI) were brought from Sinopharm Chemical Reagent Co., Ltd., Shanghai, China. All chemical reagents were analytical grade and directly used without any further treatment.

3.2. Preparation of Photocatalysts

3.2.1. Preparation of BiOX (X = Cl, Br, and I)

In this experiment, BiOX (X = Cl, Br, I) was prepared by a facile soft liquid deposition method, as reported in our previous works [27,49–51]. 24 mmol of $Bi(NO_3)_3{\cdot}5H_2O$ was dissolved into 240 mL of ethylene glycol solution (EG) to obtain solution A at room temperature. Then, 24 mmol of KX (X = Cl, Br, and I) was dissolved into 120 mL of deionized water to obtain solutions B, which was dropped slowly into the previous solution A. The mixed solution was magnetically stirred for 1 h at room temperature. Subsequently, the products were obtained by washing them with deionized water several times and dried at 60 °C for 12 h.

3.2.2. Preparation of $Bi_7Fe_2Ti_2O_{17}X$ (X = Cl, Br, and I)

BFTOX powders were synthesized by a flux method using Bi_2O_3, BiOX, Fe_2O_3 and TiO_2 as the precursor materials. KCl/NaCl, KBr/NaBr, and KI/NaI with a ratio of 1:1 were served as the molten salt. The molten salt was mixed with the solute of Bi_2O_3, BiOX, Fe_2O_3 and TiO_2 at the stoichiometric molar ratio for BFTOX (3:1:1:2). The solute concentration is about 6.25 mol% (BFTOX/(BFTOX + flux)). 10 mol% excess of BiOX over the stoichiometric ratio was added to prevent volatilization. Afterwards, three different mixtures were transferred to alumina crucibles for the high-temperature calcination. The $Bi_7Fe_2Ti_2O_{17}Cl$ (BFTOC), $Bi_7Fe_2Ti_2O_{17}Br$ (BFTOB), and $Bi_7Fe_2Ti_2O_{17}I$ (BFTOI) were obtained at the calcination temperature of 750 °C, 750 °C, and 700 °C for 6 h, respectively. After natural cooling, the obtained products were collected by filtration and thoroughly washed with the deionized water for several times. Finally, the products were dried at 60 °C for 12 h.

3.3. Characterization

X-ray diffraction (XRD) (X′ Pert3 Powder, PANalytical, Almelo, The Netherlands, $\lambda = 0.15406$ nm) was used to analyze the crystal structure of BFTOX samples with Cu Kα radiation. The sample morphologies were examined by field emission scanning electron microscope (FE-SEM) (FEI, Hillsboro, OR, USA). X-ray photoelectron spectroscopy (XPS) was carried out to investigate the chemical nature of the samples via a Thermo Scientific Escalab 250 Xi spectrometer (Thermo Fisher Scientific, Carlsbad, CA, USA). The UV-vis diffuse reflectance spectroscopy (UV-vis DRS) was attained by using a UV-2550 (Shimadzu, Kyoto, Japan). The UV-vis absorption spectra of the samples were performed by UV-2450 (Shimadzu, Kyoto, Japan).

3.4. Photocatalytic Experiments

Photocatalytic experiments of the samples were discussed with a 300 W Xenon lamp (CEL-HXF300 Beijing China Education Au-light Co., Ltd., Beijing, China) as the light source. 100 mg of photocatalysts were separately added into 100 mL of 10 mg/L MO and RhB, and then stirred in the dark for 30 min to reach adsorption-desorption equilibrium. 4 mL solution was withdrawn every 30 min. The above suspension was centrifuged and the residual concentration of dye was detected by UV-vis spectrophotometer. During the degradation process of MO and RhB over BFTOX, $\cdot OH$, h^+, and $\cdot O_2^-$ were captured by a certain proportion of *tert*-butyl alcohol (TBA, 1 mM), EDTA (1 mM), and benzoquinone (BQ, 0.25 mM), respectively.

The experiments on the reduction of CO_2 were performed in a gas closed-circulation system. Photocatalyst powders of 0.01 g were dispersed in the absolute ethyl alcohol. Then, the photocatalysts solution was coated on a glass slide and placed in a reaction chamber (1 L). Deionized water entered the reaction chamber in the form of steam, and 1000 ppm CO_2 was introduced. After the whole system was stabilized, a 300 W Xe-arc lamp was applied to simulate sunlight.

3.5. Electrochemical Measurement

Photocurrent density versus time curves and electrochemical impedance spectra (EIS) were performed by a CHI660D electrochemical analyzer (Chenhua Instruments Co., Ltd., Shanghai, China) with a standard three-electrode system, including a working electrode, a reference electrode (saturated Ag/AgCl), and a counter electrode (Pt wire). The working electrode was obtained: 5 mg of as-prepared photocatalysts were dispersed into 40 μL of naphthol to make the slurry, and the slurry was deposited on the fluorine-tin oxide (FTO)glass. Afterwards, the substrate was dried at 80 °C for 4 h and calcined in a muffle furnace at 120 °C for 1 h.

3.6. Theoretical Calculations

In this work, the calculation of DFT with the projector-augmented wave (PAW) was carried out by VASP code [53]. The generalized gradient approximation (GGA) for the electron exchange and correlation corrections used Perdew-Burke-Ernzerhof (PBE) [54] to optimize the geometric structure and the next procedures were performed within the Heyd-Scuseria-Ernzerhof screened hybrid functional (HSE) [55], including band structures. In order to obtain accurate results, the cut-off energy was set to 520 eV and the irreducible Brillouin zone grid was used to $5 \times 5 \times 1$ mesh. The energy convergence criterion was 1×10^{-4} eV as well as -1×10^{-2} eV for atomic force convergence. In addition, the magnetic moment of the Fe atom was set to 4 μB. Due to the unpredictability of the synthesized samples in the experiment, Fe and Ti alternate arrangement is used to simulate the disorder situation in this DFT calculated process.

4. Conclusions

In summary, a series of novel Sillén–Aurivillius oxygen halides, $Bi_7Fe_2Ti_2O_{17}X$ (X = Cl, Br, and I), were successfully synthesized by molten salt method for the efficient CO_2 reduction and degradation of organic pollutants. The highly dispersive O 2p band of BFTOC and BFTOB samples contributing to the VBM not only renders the VBM essentially negative, but also explains its stability against self-decomposition deactivation from theory and experiment. For BFTOI, self-oxidation deactivation of I 5p orbitals leads to inferior CO_2 reduction in BFTOI. BFTOC and BFTOB samples possess outstanding activity for CO_2 reduction to CO, and the production rates of CO are 3.74 μmol g^{-1} h^{-1} and 3.6 μmol g^{-1} h^{-1}, respectively. More importantly, the BFTOX with unique nanosheet morphology displays a superb photocatalytic performance on MO and RhB mixture degradation. The removal efficiencies of the MO and RhB for BFTOC and BFTOB are 90% and 85% higher than BFTOI, which is a result of the improved separation of photogenerated charge carriers and optical absorption. To be more specific, the radical trapping tests and possible mechanism of BFTOX for the photocatalytic degradation of MO and RhB indicated that the h^+ and $\cdot O_2^-$ were the major active species to boost photocatalytic reactions. As an attractive photocatalyst, BFTOX has promising potential for CO_2 reduction and the degradation of organic pollutants.

Supplementary Materials: The following supporting information can be downloaded at: https://www.mdpi.com/article/10.3390/catal13040751/s1, Figure S1: The SEM-EDS elemental mappings of (a) Bi, (b) Fe, (c) Ti, (d) O, and (e) Br for BFTOC sample. The SEM-EDS elemental mappings of (f) Bi, (g) Fe, (h) Ti, (i) O, and (j) Br for BFTOI sample; Figure S2: Ti 2p XPS spectrum of the BFTO-Br sample; Figure S3: O 1*s* XPS spectrum of the BFTO-Br sample; Figure S4: Degradation rate of MO/RhB over (a) BFTOC and (b) BFTOC with the addition of p-BQ, EDTA-2Na and TBA; Table S1: The average CO production rates of BFTOX at different times.

Author Contributions: J.C. and Y.G.: conceptualization, methodology, investigation, testing, editing original draft and theoretical calculation; S.X., Z.Z., Z.M., C.Z. and J.Z.: conceptualization, methodology, investigation, testing; L.S.: theoretical calculation; Y.Z.: writing—review & editing, supervision, data curation. Q.Z.: project administration, funding acquisition, writing—review & editing. All authors have read and agreed to the published version of the manuscript.

Funding: This work is supported by the National Natural Science Foundation of China (No. 12274361), the Natural Science Foundation of Jiangsu Province (BK20211361), and College Natural Science Research Project of Jiangsu Province (20KJA430004), the Postgraduate Research & Practice Innovation Program of Jiangsu Province (KYCX21_3145) and the school-level research projects of Yancheng Institute of Technology (xjr2019028, xjr2019059).

Data Availability Statement: The data presented in this study are available on request from the corresponding author.

Conflicts of Interest: The authors declare no conflict of interest.

References

1. Yan, J.; Wang, C.; Ma, H.; Li, Y.; Liu, Y.; Suzuki, N.; Terashima, C.; Fujishima, A.; Zhang, X. Photothermal synergic enhancement of direct Z-scheme behavior of $Bi_4TaO_8Cl/W_{18}O_{49}$ heterostructure for CO_2 reduction. *Appl. Catal. B Environ.* **2020**, *268*, 118401. [CrossRef]
2. Zhang, Y.; Lin, S.; Cheng, S.; He, Z.; Hu, Z.; Zhou, Z.; Liu, W.; Sun, Y. Boosting Cu(In,Ga)Se_2 Thin Film Growth in Low-Temperature Rapid-Deposition Processes: An Improved Design for the Single-Heating Knudsen Effusion Cell. *Engineering* **2021**, *7*, 534–541. [CrossRef]
3. Katsumata, H.; Islam Molla, M.A.; Islam, J.B.; Tateishi, I.; Furukawa, M.; Kaneco, S. Dual Z-scheme heterojunction g-$C_3N_4/Ag_3PO_4/AgBr$ photocatalyst with enhanced visible-light photocatalytic activity. *Ceram. Int.* **2022**, *48*, 21898–21905. [CrossRef]
4. Lu, X.; Quan, L.; Hou, H.; Qian, J.; Liu, Z.; Zhang, Q. Fabrication of 1D/2D Y-doped $CeO_2/ZnIn_2S_4$ S-scheme photocatalyst for enhanced photocatalytic H_2 evolution. *J. Alloy. Compd.* **2022**, *925*, 166552. [CrossRef]
5. Melchionna, M.; Fornasiero, P. Updates on the Roadmap for Photocatalysis. *ACS Catal.* **2020**, *10*, 5493–5501. [CrossRef]
6. Kumar, A.; Kumar, A.; Krishnan, V. Perovskite Oxide Based Materials for Energy and Environment-Oriented Photocatalysis. *ACS Catal.* **2020**, *10*, 10253–10315. [CrossRef]
7. Kumar, A.; Pathania, D.; Gupta, N.; Raj, P.; Sharma, A. Photo-degradation of noxious pollutants from water system using Cornulaca monacantha stem supported $ZnFe_2O_4$ magnetic bio-nanocomposite. *Sustain. Chem. Pharm.* **2020**, *18*, 100290. [CrossRef]
8. Arush, S.; Deepak, P.; Ajay, K. Bio-Polymer Based Tragacanth Gum (TG) Loaded Fe_3O_4 Nanocomposite for the Sequestration of Tenacious Congo Red Dye from Waste Water. *J. Mater. Sci. Technol. Res.* **2020**, *7*, 92–100. [CrossRef]
9. Sun, C.; Yang, J.; Xu, M.; Cui, Y.; Ren, W.; Zhang, J.; Zhao, H.; Liang, B. Recent intensification strategies of SnO_2-based photocatalysts: A review. *Chem. Eng. J.* **2022**, *427*, 131564. [CrossRef]
10. Xu, K.; Wang, L.; Xu, X.; Dou, S.X.; Hao, W.; Du, Y. Two dimensional bismuth-based layered materials for energy-related applications. *Energy Storage Mater.* **2019**, *19*, 446–463. [CrossRef]
11. Lu, X.; Liu, Z.; Zhao, X.; Xu, W.; Hou, H.; Qian, J. CdS Nanoparticles Decorated 1D CeO_2 Nanorods for Enhanced Photocatalytic Desulfurization Performance. *Catalysts* **2022**, *12*, 1478. [CrossRef]
12. Chandel, M.; Thakur, M.; Sharma, A.; Pathania, D.; Kumar, A.; Singh, L. Chlorophyll sensitized $(BiO)_2CO_3/ CdWO_4$/rGO nano-hybrid assembly for solar assisted photo-degradation of chlorzoxazone. *Chemosphere* **2022**, *305*, 135472. [CrossRef] [PubMed]
13. Ren, X.; Gao, M.; Zhang, Y.; Zhang, Z.; Cao, X.; Wang, B.; Wang, X. Photocatalytic reduction of CO_2 on BiOX: Effect of halogen element type and surface oxygen vacancy mediated mechanism. *Appl. Catal. B: Environ.* **2020**, *274*, 119063. [CrossRef]
14. Zhang, L.; Li, Y.; Li, Q.; Fan, J.; Carabineiro, S.A.C.; Lv, K. Recent advances on Bismuth-based Photocatalysts: Strategies and mechanisms. *Chem. Eng. J.* **2021**, *419*, 129484. [CrossRef]
15. He, R.; Cao, S.; Zhou, P.; Yu, J. Recent advances in visible light Bi-based photocatalysts. *Chin. J. Catal.* **2014**, *35*, 989–1007. [CrossRef]

16. Miao, Z.; Wang, Q.; Zhang, Y.; Meng, L.; Wang, X. In situ construction of S-scheme AgBr/BiOBr heterojunction with surface oxygen vacancy for boosting photocatalytic CO_2 reduction with H_2O. *Appl. Catal. B Environ.* **2022**, *301*, 120802. [CrossRef]
17. Meng, X.; Zhang, Z. Bismuth-based photocatalytic semiconductors: Introduction, challenges and possible approaches. *J. Mol. Catal. A Chem.* **2016**, *423*, 533–549. [CrossRef]
18. Divya, J.; Shivaramu, N.J.; Roos, W.D.; Purcell, W.; Swart, H.C. Synthesis, surface and photoluminescence properties of Sm^{3+} doped α-Bi_2O_3. *J. Alloy Compd.* **2021**, *854*, 157221. [CrossRef]
19. Zhao, Q.; Liu, X.; Xing, Y.; Liu, Z.; Du, C. Synthesizing Bi_2O_3/BiOCl heterojunctions by partial conversion of BiOCl. *J. Mater. Sci.* **2016**, *52*, 2117–2130. [CrossRef]
20. Shang, J.; Chen, T.; Wang, X.; Sun, L.; Su, Q. Facile fabrication and enhanced photocatalytic performance: From BiOCl to element-doped BiOCl. *Chem. Phys. Lett.* **2018**, *706*, 483–487. [CrossRef]
21. Han, N.; Zhang, Q. Stoichiometry-dependent photocatalytic performance of bismuth-based oxychlorides BiOyCl. *Appl. Surf. Sci.* **2021**, *562*, 150215. [CrossRef]
22. He, H.; Yin, J.; Li, Y.; Zhang, Y.; Qiu, H.; Xu, J.; Xu, T.; Wang, C. Size controllable synthesis of single-crystal ferroelectric $Bi_4Ti_3O_{12}$ nanosheet dominated with {0 0 1} facets toward enhanced visible-light-driven photocatalytic activities. *Appl. Catal. B Environ.* **2014**, *156–157*, 35–43. [CrossRef]
23. Xie, Z.; Tang, X.; Shi, J.; Wang, Y.; Yuan, G.; Liu, J.-M. Excellent piezo-photocatalytic performance of Bi4Ti3O12 nanoplates synthesized by molten-salt method. *Nano Energy* **2022**, *98*, 107247. [CrossRef]
24. Bhat, S.S.M.; Sundaram, N.G. Photocatalysis of Bi4NbO8Cl hierarchical nanostructure for degradation of dye under solar/UV irradiation. *New J. Chem.* **2015**, *39*, 3956–3963. [CrossRef]
25. Fujito, H.; Kunioku, H.; Kato, D.; Suzuki, H.; Higashi, M.; Kageyama, H.; Abe, R. Layered Perovskite Oxychloride Bi4NbO8Cl: A Stable Visible Light Responsive Photocatalyst for Water Splitting. *J. Am. Chem. Soc.* **2016**, *138*, 2082–2085. [CrossRef] [PubMed]
26. Li, S.; Wang, C.; Li, D.; Xing, Y.; Zhang, X.; Liu, Y. Bi_4TaO_8Cl/Bi heterojunction enables high-selectivity photothermal catalytic conversion of CO_2-H_2O flow to liquid alcohol. *Chem. Eng. J.* **2022**, *435*, 135133. [CrossRef]
27. Sun, J.; Han, N.; Gu, Y.; Lu, X.; Si, L.; Zhang, Q. Hole Doping to Enhance the Photocatalytic Activity of Bi4NbO8Cl. *Catalysts* **2020**, *10*, 1425. [CrossRef]
28. Zhong, C.; Kato, D.; Takeiri, F.; Fujii, K.; Yashima, M.; Nishiwaki, E.; Fujii, Y.; Koreeda, A.; Tassel, C.; Abe, R.; et al. Single Crystal Growth of Sillén–Aurivillius Perovskite Oxyhalides Bi4NbO8X (X = Cl, Br). *Inorganics* **2018**, *6*, 41. [CrossRef]
29. Kunioku, H.; Higashi, M.; Tomita, O.; Yabuuchi, M.; Kato, D.; Fujito, H.; Kageyama, H.; Abe, R. Strong hybridization between Bi-6s and O-2p orbitals in Sillén–Aurivillius perovskite Bi4MO8X (M = Nb, Ta; X = Cl, Br), visible light photocatalysts enabling stable water oxidation. *J. Mater. Chem. A* **2018**, *6*, 3100–3107. [CrossRef]
30. Sharma, A.; Kanth, S.K.; Xu, S.; Han, N.; Zhu, L.; Fan, L.; Liu, C.; Zhang, Q. Visible light driven g-C3N4/Bi4NbO8X (X Cl, Br) heterojunction photocatalyst for the degradation of organic pollutants. *J. Alloy. Compd.* **2022**, *895*, 162576. [CrossRef]
31. Kato, D.; Hongo, K.; Maezono, R.; Higashi, M.; Kunioku, H.; Yabuuchi, M.; Suzuki, H.; Okajima, H.; Zhong, C.; Nakano, K.; et al. Valence Band Engineering of Layered Bismuth Oxyhalides toward Stable Visible-Light Water Splitting: Madelung Site Potential Analysis. *J. Am. Chem. Soc.* **2017**, *139*, 18725–18731. [CrossRef]
32. Tao, X.; Zhao, Y.; Mu, L.; Wang, S.; Li, R.; Li, C. Bismuth Tantalum Oxyhalogen: A Promising Candidate Photocatalyst for Solar Water Splitting. *Adv. Energy Mater.* **2018**, *8*, 1701392. [CrossRef]
33. Majumdar, A.; Ghosh, U.; Pal, A. Novel 2D/2D g-C(3)N(4)/Bi(4)NbO(8)Cl nano-composite for enhanced photocatalytic degradation of oxytetracycline under visible LED light irradiation. *J. Colloid. Interface Sci.* **2021**, *584*, 320–331. [CrossRef] [PubMed]
34. Qu, X.; Liu, M.; Zhang, W.; Sun, Z.; Meng, W.; Shi, L.; Du, F. A facile route to construct $NiTiO_3$/Bi_4NbO_8Cl heterostructures for enhanced photocatalytic water purification. *J. Mater. Sci.* **2020**, *55*, 9330–9342. [CrossRef]
35. Shi, L.; Wu, X.; Xu, C.; Bai, Q.; Nie, Z.; Ji, C.; Zhang, Y.; Yin, Z.; Zhang, S.; Qu, X.; et al. Defect-engineering of Pt/Bi_4NbO_8Br heterostructures for synergetic promotional photocatalytic removal of versatile organic contaminants. *J. Mater. Chem. C* **2021**, *9*, 2784–2792. [CrossRef]
36. Feng, Z.; Li, G.; Yuan, X.; Zhang, Z.; Tang, M.; Zhang, R. Improved photocatalytic activity of Bi_4TaO_8Cl by Gd^{3+} doping. *J. Am. Ceram. Soc.* **2018**, *102*, 2390–2397. [CrossRef]
37. Gu, Y.; Yu, F.; Chen, J.; Zhang, Q. Facile Synthesis of Sillén-Aurivillius Layered Oxide $Bi_7Fe_2Ti_2O_{17}Cl$ with Efficient Photocatalytic Performance for Degradation of Tetracycline. *Catalysts* **2022**, *12*, 221. [CrossRef]
38. Wang, Y.; Sun, X.; Xian, T.; Liu, G.; Yang, H. Photocatalytic purification of simulated dye wastewater in different pH environments by using $BaTiO_3$/Bi_2WO_6 heterojunction photocatalysts. *Opt. Mater.* **2021**, *113*, 110853. [CrossRef]
39. Shao, L.; Xia, X.; Wei, G.; Qin, J.; Liu, Y. A dramatic enhancement of antibiotic photodegradation catalyzed by red mud-derived $Bi_5FeTi_3O_{15}$. *Sep. Purif. Technol.* **2021**, *275*, 119244. [CrossRef]
40. Yin, X.; Li, X.; Liu, H.; Gu, W.; Zou, W.; Zhu, L.; Fu, Z.; Lu, Y. Realizing selective water splitting hydrogen/oxygen evolution on ferroelectric Bi_3TiNbO_9 nanosheets. *Nano Energy* **2018**, *49*, 489–497. [CrossRef]
41. Wang, Z.; Li, C.; Domen, K. Recent developments in heterogeneous photocatalysts for solar-driven overall water splitting. *Chem. Soc. Rev.* **2019**, *48*, 2109–2125. [CrossRef] [PubMed]
42. Li, K.-L.; Lee, W.W.; Lu, C.-S.; Dai, Y.-M.; Chou, S.-Y.; Chen, H.-L.; Lin, H.-P.; Chen, C.-C. Synthesis of BiOBr, Bi_3O_4Br, and $Bi_{12}O_{17}Br_2$ by controlled hydrothermal method and their photocatalytic properties. *J. Taiwan Inst. Chem. Eng.* **2014**, *45*, 2688–2697. [CrossRef]

43. Lin, H.-P.; Lee, W.W.; Huang, S.-T.; Chen, L.-W.; Yeh, T.-W.; Fu, J.-Y.; Chen, C.-C. Controlled hydrothermal synthesis of $PbBiO_2Br/BiOBr$ heterojunction with enhanced visible-driven-light photocatalytic activities. *J. Mol. Catal. A Chem.* **2016**, *417*, 168–183. [CrossRef]
44. Zhang, Y.; Hu, Z.; Lin, S.; Cheng, S.; He, Z.; Wang, C.; Zhou, Z.; Sun, Y.; Liu, W. Facile Silver-Incorporated Method of Tuning the Back Gradient of Cu(In,Ga)Se_2 Films. *ACS Appl. Energy Mater.* **2020**, *3*, 9963–9971. [CrossRef]
45. Zhang, Y.; Hu, Z.; Lin, S.; Wang, C.; Cheng, S.; He, Z.; Zhou, Z.; Sun, Y.; Liu, W. Silver Surface Treatment of Cu(In,Ga)Se_2 (CIGS) Thin Film: A New Passivation Process for the CdS/CIGS Heterojunction Interface. *Sol. RRL* **2020**, *4*, 2000290. [CrossRef]
46. Zhang, Y.; Gao, Q.; Ao, J.; Zhang, Y.; Bi, J.; Guo, J.; Han, Y.; Sun, G.; Zhang, Y.; Liu, W.; et al. Enhancing Surface Properties for Electrodeposited Cu(In,Ga)Se_2 Films by $(NH_4)_2S$ Solution at Room Temperature. *ACS Appl. Energy Mater.* **2021**, *4*, 3822–3831. [CrossRef]
47. Qing, G.; Ao, J.; Zhang, Y.; Zhang, Y.; Guo, J.; Sun, G.; Liu, W.; Liu, F.; Zhang, Y. Pulse Selenization in Cu(In,Ga)Se_2 Solar Cells: A Promising Approach to Achieve High Efficiency by Electrodeposition. *ACS Appl. Energy Mater.* **2021**, *4*, 8322–8329. [CrossRef]
48. Makula, P.; Pacia, M.; Macyk, W. How To Correctly Determine the Band Gap Energy of Modified Semiconductor Photocatalysts Based on UV-Vis Spectra. *J. Phys. Chem. Lett.* **2018**, *9*, 6814–6817. [CrossRef]
49. Zhang, Y.; Xu, S.; Mu, Z.; Liu, K.; Chen, J.; Zhou, C.; Yao, Y.; Chen, X.; Shi, L.; Wang, Z.; et al. Simulation analysis of Cd-free Cu(In,Ga)Se_2 solar cells with novel BiOX (X=Cl, Br) buffer layers. *Vacuum* **2022**, *206*, 111569. [CrossRef]
50. Xu, S.; Zhang, Y.; Wang, Y.; Chen, J.; Zhou, C.; Mu, Z.; Zhang, Z.; Zhang, J.; Wang, J.; Zhang, Q. Coupled Ferroelectric Polarization in Novelty Sillén–Aurivillius $BaBi_4TiNbO_{11}Cl$ Material for Photocatalysis. *J. Alloy Compd.* **2023**, *954*, 169932. [CrossRef]
51. Han, N.; Xu, S.; Zhang, Q. Flux synthesis of Bi_2MO_4Cl (M = Gd and Nd) nanosheets for high-efficiency photocatalytic oxygen evolution under visible light. *J. Mater. Sci.* **2022**, *57*, 2870–2882. [CrossRef]
52. Wang, S.; Teng, F.; Zhao, Y. Effect of the molecular structure and surface charge of a bismuth catalyst on the adsorption and photocatalytic degradation of dye mixtures. *RSC Adv.* **2015**, *5*, 76588–76598. [CrossRef]
53. Kresse, G.; Hafner, J. Ab initio molecular dynamics for liquid metals. *Phys. Rev. B Condens. Matter.* **1993**, *47*, 558–561. [CrossRef]
54. Perdew, J.P.; Burke, K.; Ernzerhof, M. Generalized gradient approximation made simple. *Phys. Rev. Lett.* **1996**, *77*, 3865. [CrossRef] [PubMed]
55. Heyd, J.; Scuseria, G.E.; Ernzerhof, M.J. Hybrid functionals based on a screened Coulomb potential. *J. Chem. Phys.* **2003**, *118*, 8207–8215. [CrossRef]